JOURNAL OF SYNCHROTRON RADIATION

ISSN 1600-5775

Received 7 June 2019
Accepted 3 September 2019

Edited by S. M. Heald, Argonne National Laboratory, USA

Keywords: X-ray emission spectroscopy; time-resolved; pump/probe; synchrotron; beryllium lenses; solution dynamics; MHz repetition rate.

Supporting information: this article has supporting information at journals.iucr.org/s

Micro-focused MHz pink beam for time-resolved X-ray emission spectroscopy

Ming-Feng Tu,[a,b]* Gilles Doumy,[a]* Andre Al Haddad,[a,c] Anne Marie March,[a] Stephen H. Southworth,[a] Lahsen Assoufid,[d] Yoshiaki Kumagai,[a] Donald A. Walko,[d] Anthony D. DiChiara,[d] Zunping Liu,[d] Bing Shi,[d] Linda Young[a] and Christoph Bostedt[a,b,c,e]

[a]Chemical Sciences and Engineering Division, Argonne National Laboratory, USA, [b]Department of Physics and Astronomy, Northwestern University, USA, [c]Laboratory for Femtochemistry, Paul Scherrer Institut (PSI), Switzerland, [d]Advanced Photon Source, Argonne National Laboratory, USA, and [e]LUXS Laboratory for Ultrafast X-ray Sciences, Institute of Chemical Sciences and Engineering, École Polytechnique Fédérale de Lausanne (EPFL), Switzerland. *Correspondence e-mail: mtu@anl.gov, gdoumy@anl.gov

The full radiation from the first harmonic of a synchrotron undulator (between 5 and 12 keV) at the Advanced Photon Source is microfocused using a stack of beryllium compound refractive lenses onto a fast-moving liquid jet and overlapped with a high-repetition-rate optical laser. This micro-focused geometry is used to perform efficient nonresonant X-ray emission spectroscopy on transient species using a dispersive spectrometer geometry. The overall usable flux achieved on target is above 10^{15} photons s^{-1} at 8 keV, enabling photoexcited systems in the liquid phase to be tracked with time resolutions from tens of picoseconds to microseconds, and using the full emission spectrum, including the weak valence-to-core signal that is sensitive to chemically relevant electronic properties.

1. Introduction

Hard X-ray spectroscopies have developed as powerful tools to probe the electronic and geometric structure of molecules in complex and disordered system (Glatzel & Bergmann, 2005). Their elemental sensitivity allows for selective probing of structure in the vicinity of the absorbing atom. Their high penetration power makes high-vacuum conditions unnecessary and *in situ/operando* studies feasible. Combined in a pump–probe scheme with short laser pulses, time-resolved X-ray spectroscopy can follow the evolution of structural and electronic changes induced by the photoexcitation (Kraus *et al.*, 2018). Laser-pump/X-ray-probe spectroscopy was pioneered using X-ray absorption spectroscopy (XAS) and the high-power lasers available at the time, which operated at kHz repetition rates (Chen *et al.*, 2014; Milne *et al.*, 2014; Chergui & Collet, 2017). With the advent of high-power MHz repetition rate pump lasers, pump–probe cycling could be done using all of the MHz repetition rate X-ray pulses from the synchrotron (March *et al.*, 2011; Lima *et al.*, 2011; Britz *et al.*, 2016). This allowed for use of more flux-demanding X-ray spectroscopies, such as nonresonant X-ray emission spectroscopy (XES) (Vankó *et al.*, 2013; Penfold *et al.*, 2018). Pump–probe XES developed concurrently at X-ray free-electron laser (XFEL) facilities, where high X-ray flux is available in broad bandwidth, intense, low repetition rate (120 Hz) X-ray pulses (Zhang *et al.*, 2014; Kern *et al.*, 2014). These developments at synchrotrons and XFELs demonstrated the value of XES for understanding photoinduced molecular structure

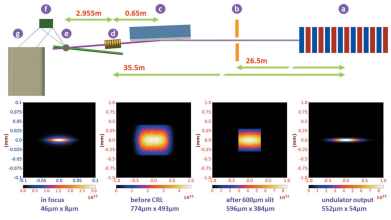

changes. For transition metal systems, information about spin state and covalency provided by $K\alpha$ and mainline $K\beta$ XES complemented well the information about oxidation state, cooordination geometry and symmetry provided by XAS.

Hard X-ray nonresonant emission from orbitals lying higher than the inner shells (*e.g.* 2*p* and 3*p*) has also been recognized as valuable for understanding structural changes. So-called valence-to-core (VTC) XES provides a view of the occupied valence orbitals from the perspective of the metal center, complementing the information on unoccupied orbitals provided by XAS (Pollock & DeBeer, 2015; Bauer, 2014; Lee *et al.*, 2010; Gallo & Glatzel, 2014; Smolentsev *et al.*, 2009). VTC XES has been shown to overcome limitations of XAS in identifying ligand atoms with similar atomic number (*e.g.* O, C, N) (Lancaster *et al.*, 2011). Together, XAS and XES spectroscopies can provide a great deal of information about the valence orbitals that are involved in bonding and chemical processes.

A challenge for the use of VTC XES is its very weak signal strength, which is typically hundreds of times smaller than the $K\alpha$ lines. We demonstrated laser-pump/X-ray-probe VTC XES at the Advanced Photon Source (APS) in a study of the short-lived photoinduced high spin state of the Fe(II) complex $[Fe(terpy)_2]^{2+}$. Using the X-ray flux of 10^{12} photons s^{-1} in the monochromatic beam at 7-ID-D and a multi-crystal X-ray spectrometer to maximize the collection efficiency of the emission signal, we collected time-resolved VTC XES, concurrently with the $K\alpha$ and mainline $K\beta$ lines, with sufficient signal-to-noise to detect the theoretically predicted changes in the high-spin VTC XES lineshape (March *et al.*, 2017). The accumulation time required, however, was 20 h, indicating that 10^{12} photons s^{-1} is insufficient for making pump–probe VTC XES practical for a wide variety of systems.

Since narrow-bandwidth X-rays are not a requirement for nonresonant XES (the X-ray energy only needs to be above the absorption edge), a straightforward means of dramatically increasing the X-ray flux is to forgo the monochromator. Use of the full first harmonic of the synchrotron undulator radiation (so-called pink beam) is established for imaging (King *et al.*, 2016; Meents *et al.*, 2017; Martin & Koch, 2006) and scattering (Skuza *et al.*, 2007) applications. For time-resolved studies, pink-beam operation has been limited to 1 kHz, with an average flux of about 10^{13} photons s^{-1} (Wullf *et al.*, 2003; Graber *et al.*, 2011). Application of pink-beam X-rays to MHz repetition rate pump–probe studies requires a means of focusing the X-rays to a micro-focused spot while managing the high heat load imposed by the high-power X-rays. The microfocus ($\sim$10 µm) is needed to allow a fast-flowing liquid jet ($\sim$60 m s^{-1}) to refresh the sample volume between pump–probe cycles. It is worth mentioning that a high repetition rate for the laser excitation necessarily limits the range of lifetimes that can be studied, although reducing the repetition rate and the flow speed is possible to extend this range. The microfocus has the additional advantage of allowing for use of pump lasers with limited pulse energies ($\sim$µJ), since small laser spots can be used to produce high laser fluences required for efficient excitation of the sample. Two main options were considered: (*a*) using a pair of water-cooled elliptical mirrors in a Kirkpatrick–Baez (KB) configuration (Reininger *et al.*, 2015) or (*b*) a combination of a flat, water-cooled harmonic rejection mirror and a water-cooled stack of beryllium compound refractive lenses (CRLs) (Dufresne *et al.*, 2016). The KB mirrors are attractive due to their achromatic focusing properties with photon energy. With the right choice of coatings and grazing-incidence angle, efficient harmonic suppression is achieved in a sub-2 µm FWHM focus in the vertical direction, with full tunability between 5 and 10 keV. However, such an optical system is quite expensive, and requires permanent installation at a beamline, a much more ambitious goal than our present demonstration. The CRL option forces some strong compromises due to the chromaticity of the optics, but allows for a simpler and cost-effective system better suited to our needs.

In this paper, we describe our implementation of micro-focused, MHz pink-beam X-rays at 7-ID-B for laser-pump/X-ray-probe, nonresonant XES measurements of photo-excited molecules in solutions (see Fig. 1). The X-rays can be tuned from about 5 keV to 12 keV, allowing access to the *K*-edges of all 3*d* transition metals, as well as the *L*-edges of lanthanides and 5*d* transition metals. Measurement of time-resolved core-to-core emission lines (*e.g.* $K\alpha$ and mainline $K\beta$) can be done with excellent signal-to-noise in minutes, even for dilute ($\sim$1 m*M*) samples. The high X-ray flux (10^{15} photons s^{-1}) enables the application of time-resolved VTC XES for a wide variety of solution phase systems.

2. Micro-focused pink beam

In this section, we discuss the design constraints that resulted in the setup presented in Fig. 1, and present results from simulations and measurements of its focusing properties with the undulator's first harmonic centered at 8 keV, chosen to provide photons well above the *K*-edge of iron (7.1 keV), since we used iron-based complexes as tests for XES spectroscopy. Beamline 7-ID at the APS is equipped with a standard undulator A (3.3 cm period) producing a total radiation output of kilowatts (Walko *et al.*, 2016). As such, care has to be taken regarding heat load on the transport and focusing optics necessary to produce the pink-beam X-ray microfocus.

2.1. Design of the harmonic rejection mirror

The role of the harmonic rejection mirror is to selectively reflect the undulator's first harmonic, while the higher harmonics are deposited into the mirror substrate, by adjusting the angle of incidence. To reduce the heat load on the CRLs, the mirror is the first optic placed after the white-beam slits. Taking into account the beam divergence, the source point to CRLs distance, and the 800 µm clear aperture of the CRLs, the white-beam slits were set to 600 µm × 600 µm. The calculated spectrum of the radiation through those slits is plotted in Fig. 2, with a first harmonic peak at 8 keV, and the flux numbers are reported in Table 1.

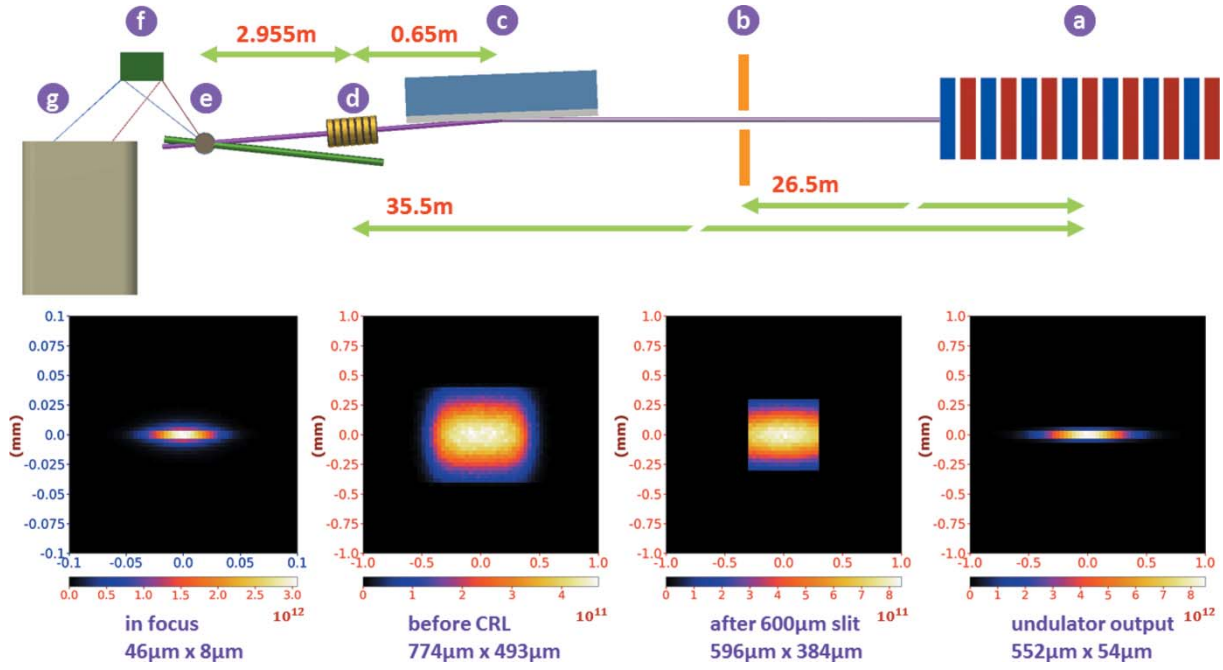

Figure 1
Beamline layout. Apparatus from right to left: (*a*) APS undulator A (3.3 cm period), (*b*) main beam-defining slit (0.6 mm × 0.6 mm), (*c*) Rh-coated (10 nm-thick) water-cooled Si mirror, (*d*) seven-stack Be compound refractive lenses of 200 μm radius of curvature, (*e*) HPLC-backed liquid jet sample, (*f*) von Hamos crystal spectrometer, and (*g*) Pilatus 100K detector. The beam profiles are simulations by ray-tracing software *McXtrace*. Note that the scale for the focused beam plot is an order of magnitude smaller.

A single 10 nm layer of rhodium was deposited on a silicon flat substrate that was 150 mm long, 35 mm wide and 30 mm high, and polished to a surface slope error of 86 nrad RMS, and height error 0.91 nm RMS. By setting the mirror to 6 mrad grazing-incidence angle, the full beam coming from the white-beam slits is easily accommodated. Theoretical reflectivity properties are presented in Fig. 2 and in Table 1, as obtained through the CXRO website (http://www.cxro.lbl.gov/) (Henke *et al.*, 1993). High reflectivity of 84% for the first harmonic at 8 keV and strong harmonic rejection are expected. The corresponding calculated spectrum impinging on the CRLs is thus plotted in Fig. 2.

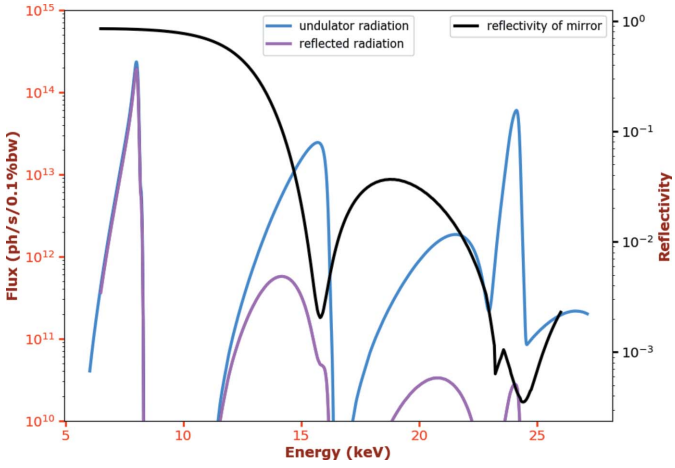

Figure 2
Spectrum simulation of APS undulator A through a 0.6 mm × 0.6 mm main slit (first-harmonic peak set at 8 keV), reflectivity of a single-layer deposit of 10 nm Rh on the silicon substrate with 6 mrad (0.34°) incident angle assuming a perfect optic and radiation spectrum after rejection mirror. Higher harmonics are significantly suppressed.

The mirror is used in a horizontally deflecting geometry in order to simplify the mechanical setup and keep the beam height constant. As a result, the power is quite concentrated in the vertical direction. Heat dissipation and its effect on the mirror properties were concerns. Simulations of temperature distribution and substrate deformation, with and without water cooling of the substrate, demonstrated the necessity of active cooling, but also showed that it should be sufficient to prevent degradation of the optical properties of the mirror. More details and some results of the simulation, as well as pictures of the actual water-cooled mirror heat sink holder, are presented in the supporting information. Varying the angle of incidence between 5 mrad and 9 mrad would accommodate the range from 12 to 5 keV, respectively, providing $\geq$ 70% reflectivity in the first harmonic with strong higher harmonic rejection, while matching the CRL acceptance. We note that adding a second mirror would essentially eliminate the higher harmonics and provide a constant beam displacement, but at the expense of a significantly more complex setup.

2.2. CRL focusing

CRLs are stacks of lenses with a focal length $f \simeq R/(2\delta N)$ where R is the radius of curvature, N is the number of lenses, and δ is the index of refraction decrement (*i.e.* $n = 1 - \delta$). The lenses employed in this project are biconcave with rotationally

Table 1
Calculated photon flux and power for the first three harmonics along the setup; also shown is the efficiency of the various elements (reflectivity for mirror, transmission for the other elements).

Harmonic (photon energy)	Flux at slits (photons s^{-1})	750 µm Be	Mirror	CRLs	Air path	Flux on target (photons s^{-1})
First (8 keV)	8.8×10^{15} (11.0 W)	0.87	0.84	0.51	0.82	2.7×10^{15} (3.3 W)
Second (16 keV)	2.2×10^{15} (5.4 W)	0.97	2.8×10^{-3}	0.83	0.98	4.8×10^{12} (11.7 mW)
Third (24 keV)	1.3×10^{15} (5.0 W)	0.98	5.4×10^{-4}	0.87	0.99	6.0×10^{11} (2.3 mW)

parabolic profiles (Snigirev *et al.*, 1996; Lengeler *et al.*, 2005) capable of focusing in two dimensions. Low-Z elements for CRLs material are beneficial for minimizing absorption, and beryllium has recently been used to produce high-quality optics. We used lenses from RXOPTICS (https://www.rxoptics.de/). Refractive lenses have strong chromatic dependence because δ is inversely proportional to the square of the photon energy. However, as was shown by Dufresne *et al.* (2016), the natural width of an undulator harmonic represents a small enough energy band that aberrations can be acceptable, and foci of the order of 10 µm FWHM, compatible with MHz time-resolved X-ray measurements, can be achieved in the vertical direction at synchrotrons for photon energies in the 5–10 keV range using a relatively small number of lenslets ($\leq$10).

We used a Monte Carlo ray-tracing X-ray beamline simulation software (*McXtrace*) to guide the design of our experimental setup (Bergbäck Knudsen *et al.*, 2013). In particular, we wanted to strike a compromise between flux, spot size and working distance considering the available motorized tables in the 7-ID-B hutch, while being able to cover most of the energy range of the undulator's first harmonic. A quick estimate shows that about half of the first-harmonic power is absorbed in the lens stack, implying the necessity of water cooling. We adapted the mechanical setup from JJ-X-ray used by Dufresne *et al.* (2016), which was meant for 1D-focusing cylindrical lenses, by building a copper holder that could accommodate up to ten lenses, thus limiting the total number of lenses one can use. A smaller radius of curvature produces a stronger lens, but reduces the acceptance. In addition, since we intend to approximately compensate for the chromaticity by adding or removing lenses, stronger lenses do not provide fine enough adjustments, especially in the 5–10 keV range where the chromaticity is strongest. We thus chose to use lenses with 200 µm radii of curvature.

Our simulations confirmed that CRLs easily produce a vertical focus of around 10 µm FWHM (see Fig. 1), but that adding more lenses does not lead to further decrease in the spot size as aberrations dominate (see the supporting information). While adding lenses slightly reduces the horizontal spot size, the increased absorption reduces the available flux. Eventually, we found that, by using a working distance of around 3 m between the lenses and the focus, we can use five lenses for about 5 keV, seven lenses for about 8 kev, and ten lenses for about 10 keV, with very similar focusing properties.

With the parameters selected from the simulated properties, a flux estimate on target can be made, taking into account the beryllium windows permanently installed on the 7-ID beamline, the white-beam slits opening, the harmonic rejection mirror reflectivity, the CRLs absorption, and the short air path right before the interaction region necessary to insert optical laser optics when performing time-resolved pump–probe experiments. Table 1 summarizes the calculations for the first three harmonics, with the first harmonic set at 8 keV. The first conclusion is that our setup should translate into a three-order-of-magnitude gain in average flux compared with using monochromatic beam (Walko *et al.*, 2016). Second, while harmonic rejection is very efficient and the contrast is around three to four orders of magnitude for the second and third harmonics, there is still a significant average flux in the higher harmonics, such that we need to pay attention to a possible contamination in the emission spectrum. It is important to note that the focused beam represents such a high X-ray fluence that it is unrealistic to use it on solid targets without rapidly damaging the sample, but we will show that it is well compatible with a fast-flowing liquid jet.

2.3. Focusing procedure and characterization

In order to evaluate the performance of our micro-focused pink-beam beam and the effectiveness of the heat load management, we imaged the beam using a cerium-doped LYSO crystal (10 mm × 10 mm × 0.15 mm) positioned at normal incidence in the direct beam at the desired focal distance. A 45° mirror placed behind the scintillator was used to image the light emitted by the scintillator onto a CCD, by way of a long-working-distance objective (Mitutoyo) and a tube lens. Using sets of simple metal foil filters positioned in the section with an air path, one could safely reduce the heat load on the crystal and ensure a reliable measurement (Kastengren, 2019).

The incident white-beam properties were determined before the harmonic rejection mirror was inserted by placing the scintillator in the direct beam. The mirror was housed in a small vacuum chamber mounted on a rotation stage to adjust the angle of incidence and a translation stage moving perpendicularly to the incident beam. Fine positioning in the vertical direction is performed using the motorized optical table where the mirror setup is attached. Alignment of the rejection mirror was then set using an imaging paddle that can be inserted between the mirror and the CRLs. It consisted of a similar scintillator as used for focus imaging, preceded by metal filters, and was imaged through a vacuum viewport using a conventional camera objective and a CCD. The flatness of

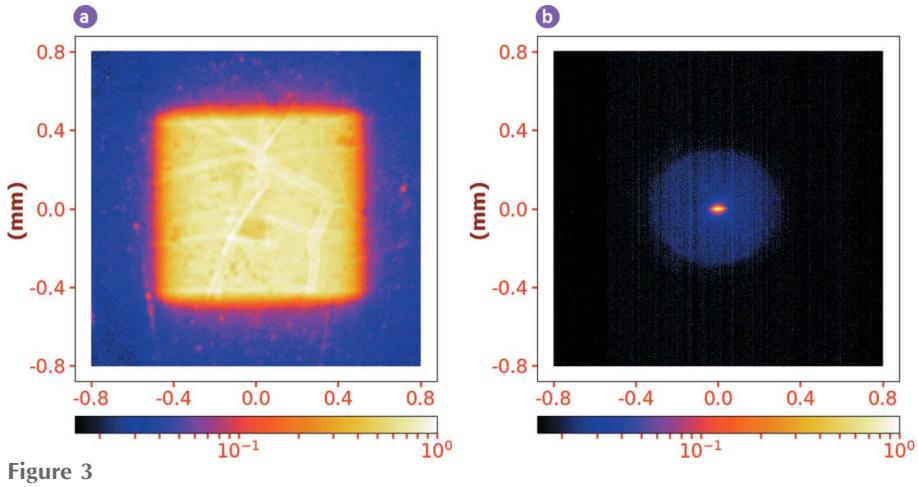

Figure 3
Beam characterization using scintillator. (*a*) Unfocused beam after reflection on harmonic rejection mirror and 3 m propagation. The structure present inside the beam is due to cracks in the scintillator crystal. (*b*) Focused beams using CRLs. The bright center spot represents the first harmonic, while the broader circular background is the loosely focused higher harmonics.

the mirror and the efficacy of the water cooling were verified by observing no alteration of the geometrical beam properties through reflection at 6 mrad grazing incidence [see Fig. 3(*a*)]. The CRLs were then inserted by translating them into the beam. The CRL vacuum chamber provides five degrees of motion (*X*, *Y* and *Z* translations as well as pitch and yaw around the beam direction). Alignment was rather easy and quick, but required strongly attenuating the beam before the scintillator crystal. Aluminium is a good choice to attenuate the first-harmonic radiation which dominates the beam after the harmonic rejection mirror. However, as indicated in the previous section, there is still a large average flux in the second harmonic, which can saturate the scintillator. Using another metal filter with a *K*-edge above the first harmonic makes it possible to study the contribution of the higher harmonics. In our case, we used copper foil in addition to aluminium. Combining filters to obtain about three orders of magnitude attenuation in the first harmonic and one order of magnitude attenuation in the second harmonic (300 µm Al, 25 µm Cu), one can distinctly observe the strongly focused first-harmonic spot as well as the loosely focused second-harmonic spot on the scintillator image shown in Fig. 3; that can be used as an alignment fiducial. When the alignment of the CRLs is correct, the different harmonics present in the focused beam co-propagate along the same direction. Otherwise the chromaticity of the lenses induces an angular shift between harmonics if the CRLs are not perfectly on axis. In addition, akin to order-sorting apertures following focusing zone plates, one could use an aperture to reduce the unfocused residual higher harmonics even more.

For a given distance between the CRLs and the interaction point, one can optimize the focusing properties by tuning the incident photon energy, since our priority is to produce a beam as small as possible in the vertical direction. This is illustrated in Fig. 4, where the measurements of the spot size in both directions are compared with the simulations. While our simulations and measurements differ quantitatively, likely due to a combination of oversimplified assumptions for the optics and uncertainty on the X-ray spectrum, their agreement is sufficient to gain confidence in the simulations to design our setup.

3. X-ray emission spectrum

In this section, we describe the application of our micro-focused pink-beam setup for performing time-resolved non-resonant X-ray emission spectroscopy with tens of picosecond time resolution. Following the demonstration of the focusing properties and flux of the setup in the previous section, we were left with several questions. With this very high X-ray average flux at MHz repetition rate, can we collect an unperturbed XES spectrum from a liquid jet target? Is the harmonic rejection sufficient to neglect possible excitations resulting from higher-energy photons? Can we successfully transfer our established methods for time-resolved X-ray spectroscopy from the monochromatic to the pink-beam case? Can we efficiently collect complete time-resolved XES spectra from low to moderate concentration solutes? We demonstrate our successful implementation by first comparing a static XES spectrum from iron (II) hexacyanide with published data obtained at 7-ID in monochromatic mode (Ross *et al.*, 2018), and then measuring the transient XES spectra of photoexcited iron(II) tris-bipyridine, capturing the spectroscopic properties of the high-spin state following optical excitation and comparing results with our previous studies (Vankó *et al.*, 2013; March *et al.*, 2017).

Non-resonant hard X-ray emission spectroscopy of molecules in solution can accommodate a moderate energy resolution around 1 eV, offering two main measurement

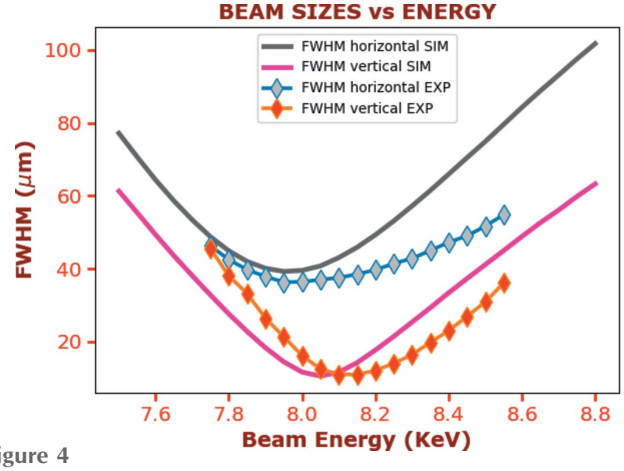

Figure 4
Horizontal and vertical beam size as a function of photon beam energy at fixed distance. CRLs assembly: seven Be lenses with 200 µm radius of curvature; distance: 2.955 m. Solid curves are simulations with *McXtrace*, diamond marks are beam measurements.

approaches. The first involves a dispersive geometry, requires a 1D or 2D detector, and allows capturing a wide spectrum with no moving parts in the spectrometer. In most cases, this approach provides the most efficient way to capture the XES spectrum, and is thus attractive for time-resolved studies. When performing laser-pump/X-ray-probe measurements, it is necessary though to gate the detector to only count signals from a subset of the entire X-ray pulse train, corresponding to X-ray pulses with a fixed delay relative to the laser pump. This is performed using a Pilatus 100K detector (Dectris), as described by Haldrup *et al.* (2012). For Fe *K*-edge emission, we used the von Hamos geometry, with two 100 mm × 25 mm cylindrically curved crystals – Ge(440) crystal for $K\alpha$, Si(531) crystal for $K\beta$ and VTC – mounted side by side such that the entire XES spectrum fits on a single position-sensitive detector. The 250 mm radius of curvature of the crystals provides a relatively large solid angle of collection, but at these emission energies the energy resolution is limited by the pixel size on the detector (172 µm). Newer detectors based on the Medipix3 chip (55 µm) would alleviate this concern.

The second approach is a scanning spectrometer, where an analyzer crystal is used to reflect a single photon energy, and an emission spectrum can be measured by varying the angle of incidence and moving the detector accordingly. We installed a scanning spectrometer in the Johann geometry, with one 10 cm-diameter spherically bent Ge(440) crystal and an avalanche photodiode (APD) detector positioned on a 1 m-diameter Rowland circle arrangement. This spectrometer can efficiently collect Fe $K\alpha$ emission, compared with a von Hamos dispersive setup, when only a single fluorescence photon energy is recorded. Crucially, the APD is a very fast detector that can be used with our MHz data acquisition (DAQ) system used for capturing the pump–probe signals (March *et al.*, 2011). The APD signal is treated by a constant-fraction discriminator and is operated in photon-counting mode with very low noise. Our DAQ is capable of tallying separately X-ray emission counts from subsets of the X-ray pulse train corresponding to specific delays between laser and X-rays. In particular, it can simultaneously capture signals from unexcited (OFF) molecules and from excited (ON) molecules at different delays after the excitation (including subsequent X-ray pulses in a pump–probe–probe scheme). As such, this provides real-time feedback on the time-resolved signal, and thus a simple way to optimize the setup (laser/X-ray overlap, time delay, *etc.*).

3.1. Static XES of iron(II) hexacyanide

Our first test of the pink-beam setup for static XES consisted of a comparison with published data on $[Fe(II)CN_6]^{4-}$ using monochromatic beam at 7.5 keV (Ross *et al.*, 2018). Results are presented in Fig. 5, where the two scaled full Fe *K*-edge XES measured with the same von Hamos crystals are compared, and in Table 2 where the relevant parameters for the two measurements are detailed, in order to perform a quantitative signal strength comparison. Identical crystal optics were used in both cases, and the first conclusion

Table 2
Experimental conditions for static measurement of 400 m*M* aqueous solution of $[Fe^{II}(CN)_6]^{4-}$.

	Monochromatic beam	Pink beam
Jet thickness	200 µm flat jet at 45°	130 µm cylindrical jet
Acquisition time	81 min	1 s
X-ray spot size	5 µm × 5 µm	40 µm × 12 µm
Detector	Mythen (55 µm pixels)	Pilatus 100K (172 µm pixels)

is that the $K\alpha$ and $K\beta$ spectral shapes are very consistent, indicating that we do not observe damage with the high average flux. Acquisition times, however, were strikingly different: 1 s with pink beam against 81 min with monochromatic beam. The data presented in Fig. 5 are scaled such that an easy incident flux comparison can be made. First, geometrical effects are corrected, taking into account the different liquid jet geometries and the different pixel sizes between the detectors that were used in both cases. Then, counts per second of acquisition are scaled to match the signal strength, with the proportionality factor yielding the ratio in available flux between the two cases. For the monochromatic cases

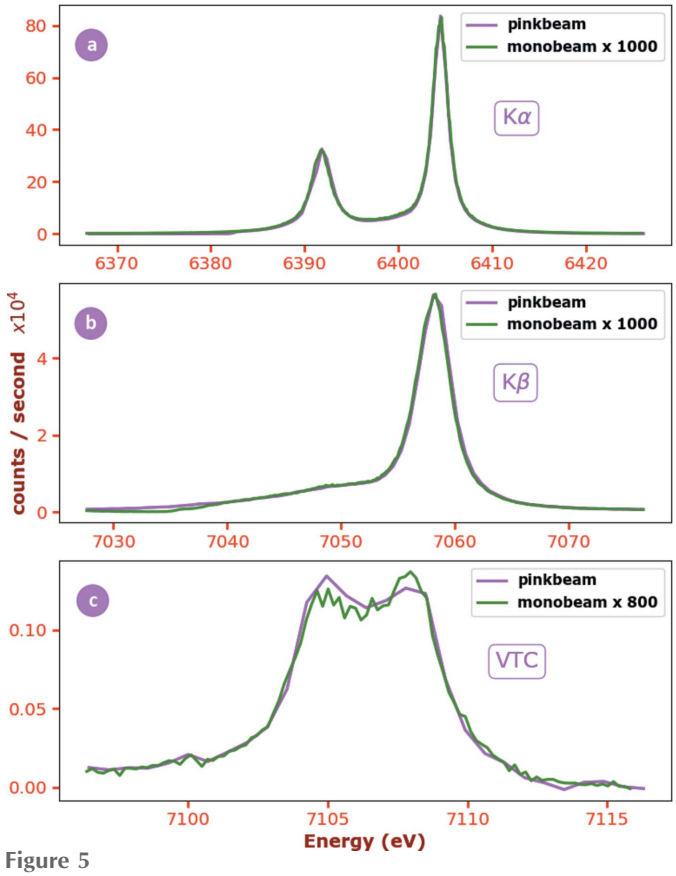

Figure 5
Comparison of static XES measured with the von Hamos spectrometer in iron (II) hexacyanide with pink beam (pink, 1 s integration) and with monochromatic beam (green, 80 min integration). (*a*) $K\alpha$, (*b*) $K\beta$ and (*c*) VTC. The scaling indicated in each panel directly reflects the average flux difference (see text for details). The small discrepancy with the VTC scaling is thought to be due to non-uniform background radiation shielding in the case of the 1D-array detector used for the static experiment.

(Khozu monochromator using diamond 111 crystals), the measured flux at 7.5 keV was 2×10^{12} photons s^{-1}. Our data then indicate an average flux of about 2×10^{15} photons s^{-1} in our focused pink beam, in good agreement with the estimate presented on Table 1.

3.2. Time-resolved XES of photoexcited iron(II) tris(2,2′-bipyridine)

To demonstrate the full feasibility of high-repetition-rate pink-beam time-resolved XES measurements and to establish its capabilities, we chose to use the prototypical iron(II) tris-bipyridine {$[Fe^{II}(bpy)_3]^{2+}$}, which has been extensively studied previously, including for the first time-resolved MHz XES experiments (Haldrup *et al.*, 2012). Following optical excitation, it quickly (∼100 fs) evolves from its metal-to-ligand charge transfer state into a high-spin quintet-excited state (Bressler *et al.*, 2009). This sample has been shown to be especially robust to both optical and X-ray exposure, yields high excitation fractions and thus large XES difference signals, and as such represents an excellent test bed for our setup. Specifically, we used a solution of acetonitrile, where the high-spin state has been characterized with a lifetime of 960 ps (Jamula *et al.*, 2014), and an excitation wavelength of 355 nm, known to excite the metal-to-ligand charge transfer state that evolves into the high-spin quintet.

The pink-beam X-rays operated as described in the previous section, using the standard operating mode at the APS consisting of 24 electron bunches separated by 153 ns circulating around the storage ring at 271 kHz, with regular top-up of the decaying bunches to keep the total storage ring current around 100 mA. This produces a train of X-ray pulses at a repetition rate of 6.5 MHz. 355 nm light was obtained by frequency-tripling our high-repetition-rate 10 ps-long laser (Duetto, Lumentum). The laser was synchronized to the storage ring, and the laser repetition rate was set at 1.3 MHz, *i.e.* each laser pulse can be overlapped with every fifth X-ray pulse. Gating the detection on a subset of the X-ray pulses allows for separating the signal from X-ray pulses at a fixed delay relative to the laser. With this specific laser repetition rate, the signal probing the shortest time after laser excitation is thus originating from about 20 mA of beam current. One attractive feature of using the fifth sub-harmonic of the X-ray repetition rate is that the laser pulse keeps a fixed delay with X-ray pulses that end up originating from each of the 24 electron bunches (as opposed to X-ray pulses originating from one or a subset of the 24 bunches). This removes the need for a gated incident X-ray intensity monitor, simplifying the setup. In order to match the laser spot shape and size to the X-ray spot measured previously, we positioned a cylindrical lens telescope ($f = -50$ mm and $f = +150$ mm) before our spherical focusing lens ($f = +300$ mm). By expanding the beam in the vertical direction before the lens, we were able to produce a 50 µm × 17 µm FWHM elliptical beam profile at the sample position. This is slightly larger than the X-ray beam, which should ensure that only excited regions of the target are probed. In addition, this laser spot size is small enough that operating our liquid jet (Microliquids, Gmbh) target at 25 m s^{-1} is sufficient to fully refresh the sample volume between laser shots. While for $[Fe^{II}(bpy)_3]^{2+}$ this is not a concern since the decay of the excited state is much faster than the laser pulses separation, refreshing the sample volume is very important in the case of long-lived or permanent photoproducts. To produce this liquid target, the sample was circulated by a high-pressure pump at a flow rate of 25 ml min^{-1} through a 130 µm-diameter quartz nozzle to produce a cylindrical jet. The laser and the X-ray beam crossed with a small, ∼5°, angle. A total laser power of about 2 W on target was used in this experiment. Spatial overlap between the laser and X-ray beams was realized using a 50 µm-diameter tantalum pinhole with either a power meter (laser) or a PIN diode (X-ray) to measure the transmitted beams. Both beams were heavily attenuated to avoid damaging the pinhole. For the X-ray beam, attenuation similar to that for focus imaging was used. Temporal overlap was realized with ∼10 ps precision using a biased GaAs MSM (metal–semiconductor–metal) fast photodetector (Hamamatsu, G4176-03), read on a 3.5 GHz, 40 GS s^{-1} oscilloscope (Lecroy, Wavepro 735Zi). The beams were again heavily attenuated such that the signal amplitude for each beam was comparable without saturating or damaging the detector.

After positioning the liquid jet at the intersection of the X-ray and laser beams, a 10 m*M* solution of $[Fe^{II}(bpy)_3]^{2+}$ in acetonitrile was circulated and the *Kα* emission signal was captured by the Johann spectrometer. The spectrometer was set at the peak of the $K\alpha_1$ line, where signal is strongest, and also where the difference with the high-spin (HS) state is maximized (Haldrup *et al.*, 2012). This signal can then be used for fine tweaks in the spatial overlap between the two beams, and to measure the decay lifetime of the HS excited state. Fig. 6 presents the normalized difference signal between the so-called laser OFF (ground state) and laser ON (ground state mixed with high-spin excited state) signals as a function of

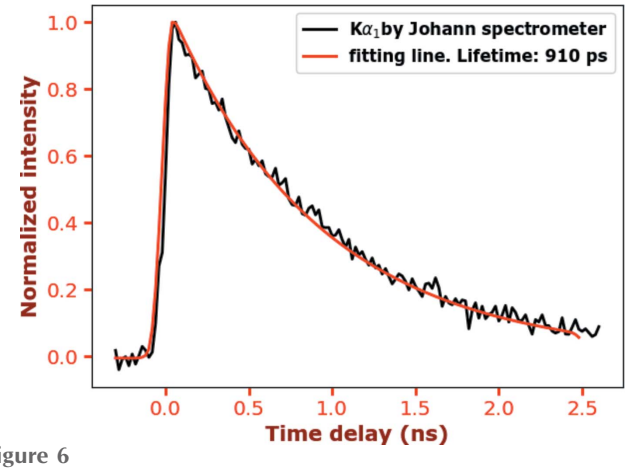

Figure 6
Normalized difference at the peak of the $K\alpha_1$ emission line between the laser-excited and ground state $[Fe^{II}(bpy)_3]^{2+}$ as a function of pump–probe delay. This is measured using the Johann spectrometer at a fixed position, using 10 ps steps for the delay, and 10 s integration per point (10 m*M* concentration). The solid line is a fit taking into account the X-ray pulse duration and the lifetime of the excited state.

delay between the laser and the X-ray pulses, collected in about 10 min. Within our time resolution, the formation of the HS state is instantaneous, so we can fit these data with a simple kinetic model with single exponential decay convoluted with a Gaussian instrument response function (IRF) dominated by the X-ray pulse temporal profile (around 80 ps FWHM with a small contribution from the 10 ps laser pulse). We thus use

$$I(t) = \int_{-\infty}^{\infty} H(t-y)\exp\left[-(t-y)/\tau\right]\mathrm{IRF}(y)\,\mathrm{d}y, \qquad (1)$$

where H is the Heaviside step function and τ stands for the lifetime of the HS state. We obtain a lifetime of 910 ps, in very good agreement with Jamula *et al.* (2014). For all subsequent measurements, we set the delay to 100 ps, corresponding to the maximum difference signal.

Using the von Hamos spectrometer and gating the Pilatus detector such that it recorded only either the laser OFF or the laser ON signal, we recorded the full Fe K-edge time-resolved XES, which is presented in Fig. 7. The top and middle panels show the $K\alpha$ and the $K\beta$ mainline, respectively. In each case, we plot the ground state (GS) and laser-excited signals, their difference, and the emission from a reference sample known to be in the HS state in the ground state {[Fe(phen)$_2$(NCS)$_2$]}. The measured difference signal shape can then be directly compared with the difference between high spin and low spin. These emission lines are not directly sensitive to the valence electrons, but are sensitive to the spin of the central ion via the intra-atomic exchange interaction in the final state of the emission process between the unpaired 3d electrons and the 2p or 3p core holes. The main effects are broadenings of the $K\alpha_1$ and $K\alpha_2$ lines, a blue shift of the main $K\beta$ line, and an intensity transfer to the $K\beta'$ satellite. The difference signals from either emission line can be used to quantitatively assess the fraction of HS state molecules in the probed volume, following the now well established method from Vankó *et al.* (2006). The absolute value of the difference signal between the HS reference and the GS spectra (each spectrum area being normalized to unity) defines the integrated absolute difference (IAD) for the complete spin change. The scaling factor obtained following the same treatment on the difference between laser-excited and GS spectra directly provides the excitation fraction γ, *i.e.*

$$\gamma = \frac{\mathrm{IAD(ON-OFF)}}{\mathrm{IAD(HS_{ref}-GS)}}. \qquad (2)$$

Using the $K\alpha$ and the $K\beta$ spectra, we obtain $\gamma_\alpha \simeq 0.57$ and $\gamma_\beta \simeq 0.53$. This excitation fraction of around 55% confirms that our micro-focused pink beam is able to efficiently probe a volume corresponding to the center of the laser-excited region, and is consistent with previous experiments with this molecule using focused monochromatic beam.

The bottom panel of Fig. 7 presents the signal in the valence-to-core region, following 200 min of acquisition. The difference signal exhibits clear signatures of the low spin to high spin transition detailed by March *et al.* (2017), chiefly an intensity reduction and a blue shift in energy that are well reproduced by calculations, as shown by the dashed curve in Fig. 7. Obtained with a single von Hamos (cylindrically bent) analyzer crystal, this result demonstrates that using high-repetition-rate pink beam fully enables time-resolved valence-to-core XES at synchrotrons.

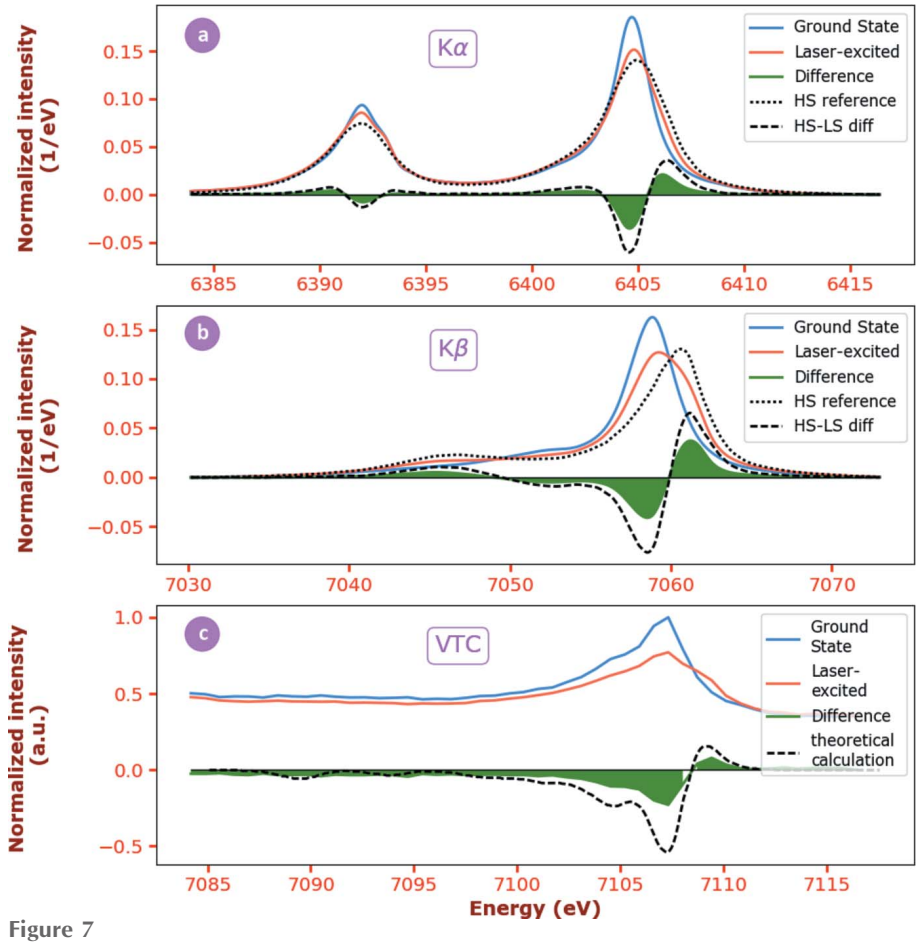

Figure 7
Full iron K-edge emission spectrum measured with the von Hamos spectrometer with high signal-to-noise quality (200 min integration). (*a*) $K\alpha$ XES of $[Fe^{II}(bpy)_3]^{2+}$ 10 mM in acetonitrile. (*b*) $K\beta$ mainline XES. Blue line: ground state. Red line: laser-excited signal at 100 ps delay. Green filled area: difference signal. The ground state and laser-excited signals were smoothed and interpolated to combine with the signal from the high-spin reference complex {[Fe(phen)$_2$(NCS)$_2$], extracted from Haldrup *et al.* (2012)}. Black dashed line: difference signal between high- and low-spin complexes, used to extract the excitation fraction in our experiment (see text). (*c*) Valence-to-core region of the XES. The raw signals are presented and compared with the result of calculations (March *et al.*, 2017).

Finally, some useful cases are presented to illustrate the potential of the setup. Fig. 8 plots the total XES spectra obtained in a single minute of acquisition (*i.e.* 30 s OFF, 30 s ON). Both the *Kα* and mainline *Kβ* signals exhibit very good signal to noise and all the major spectral features. In particular, the quality of the *Kβ* difference signal is sufficient to clearly identify the spin of the transient excited state. This result, obtained with a relatively modest concentration (10 m*M*), is very promising for a number of possible applications. The implementation of a multicrystal spectrometer (March *et al.*, 2017) would open the possibility to either use much lower concentration, such as is the norm for biological samples (Kubin *et al.*, 2017; Fransson *et al.*, 2018), or detect smaller difference signals with the same short acquisition time. The possibility to perform the measurement in a large number of excitation conditions during a single experiment allows, for example, to implement the so-called time-slicing idea, where the short excitation laser pulse is scanned inside the X-ray pulse profile and dynamics shorter than the X-ray pulse duration can be extracted (Lee *et al.*, 2013; March *et al.*, 2019).

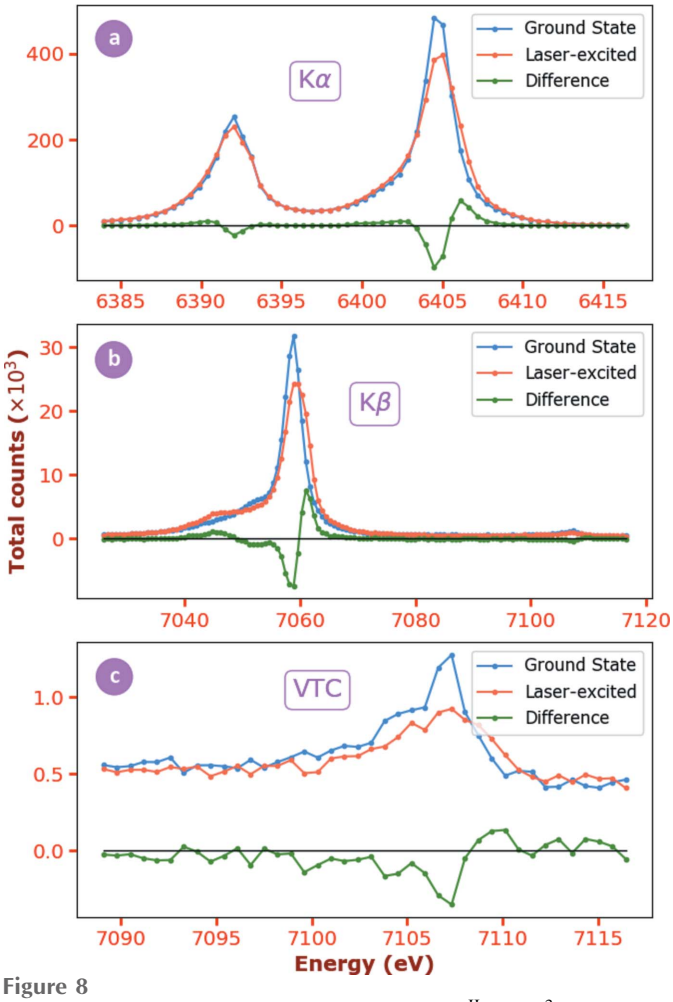

Figure 8
Raw signals from 1 min of acquisition of $[Fe^{II}(bpy)_3]^{2+}$ 10 m*M* in acetonitrile at 100 ps delay. (*a*) *Kα*, (*b*) *Kβ* full range and (*c*) VTC. The *Kα* and *Kβ* mainline XES possess sufficient signal to noise for species identification. The VTC signal shows a transient signature but requires more statistics.

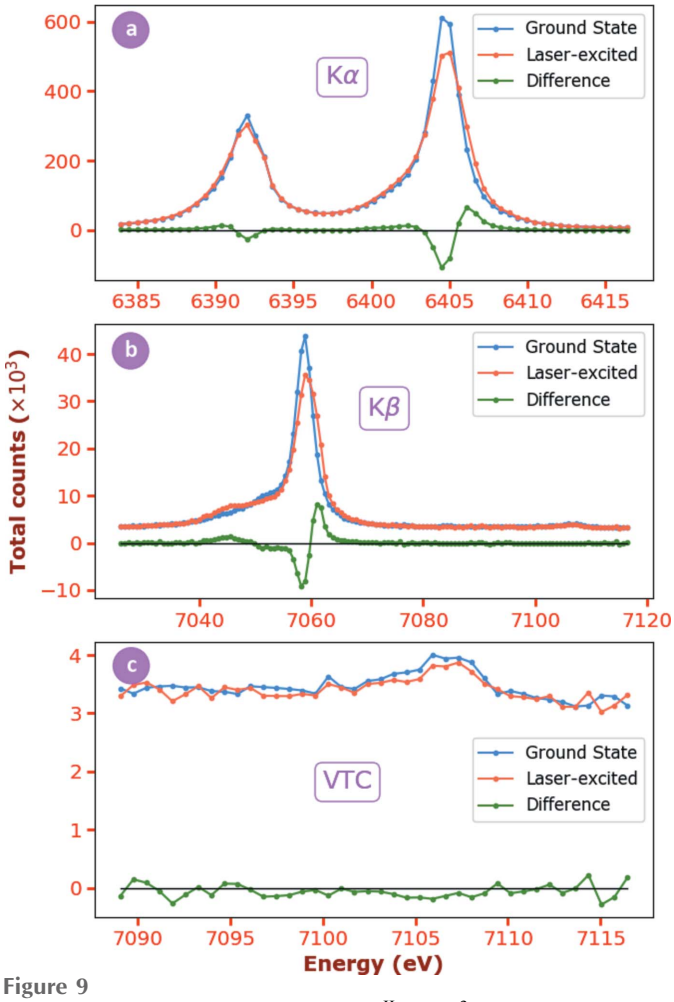

Figure 9
Raw signals for 10 min acquisition of $[Fe^{II}(bpy)_3]^{2+}$ 1 m*M* in acetonitrile at 100 ps delay. (*a*) *Kα*, (*b*) *Kβ* full range and (*c*) VTC.

In addition, for samples that exhibit strong X-ray or laser damage, or permanent photoproducts, single-pass measurements are now feasible, even without a very large quantity of sample.

At lower concentrations, signal-to-background considerations can dominate. Using our simple lead shielding, we demonstrate that our setup is easily sensitive to 1 m*M* solute concentration. Fig. 9 presents the result of 10 min acquisition (5 min OFF, 5 min ON). While the VTC region becomes barely usable, the contrast for the *Kα* and mainline *Kβ* signals is very good, such that no significant difference from the 10 m*M* case is observed.

4. Conclusion

Micro-focused pink-beam X-ray capabilities have been achieved at Sector 7 of the Advanced Photon Source. Using a simple optical setup consisting of a water-cooled harmonic rejection mirror and beryllium compound refractive lenses, a microfocused 40 µm × 12 µm FWHM elliptical spot of the undulator's first harmonic at 8 keV was measured with high harmonic contrast. Focusing properties are well reproduced by

simulation, allowing a design to easily accommodate different photon energies. The available average flux of more than 10^{15} photons s^{-1} is on par with or above the average flux that can be obtained at hard X-ray XFELs, promising a complementary hard X-ray source for studies that require a time resolution of picoseconds or above. Interestingly, as XFELs operating at high repetition rate are becoming available (European XFEL for now, and the upcoming LCLS-II), our work presents some methodologies that may be directly transposed.

A first application to nonresonant XES on a liquid target was demonstrated, with exciting new capabilities being offered now, as acquisition times are reduced by about three orders of magnitude. Besides establishing time-resolved valence-to-core XES as a viable technique on solvated systems, it is also possible to measure sensitive samples where volume recirculation is not an option. Further enhancements are currently being implemented by adding a multi-crystal von Hamos spectrometer for more efficient signal collection coupled to a higher-resolution gateable detector (Lambda 750k, X-Spectrum). While our simple setup as implemented is able to provide a micro-focused beam in the 5–12 keV range, a natural way to increase the range consists of using a multilayer monochromator with several reflective stripes. Such an improvement would allow to easily switch between monochromatic beam (crucial for X-ray absorption spectroscopy and resonant X-ray emission spectroscopy) and pink beam. Such a setup is being designed for a new beamline part of the APS-U project, the Advanced Spectroscopy Beamline, and will translate our proof of principle into a capability accessible to users.

Beyond XES, there are other applications that can benefit from nonresonant excitation. One example is Auger electron spectroscopy in the hard X-ray region, where the large incident energy bandwidth is not an issue since the Auger electron energy is fixed (Madden, 1981). Also, time-resolved X-ray liquid scattering (Ihee *et al.*, 2005), a technique that can accommodate large incident bandwidth and is often coupled to XES at XFELs since it can provide structural information complementary to the electronic information, is a natural extension of this new setup.

Funding information

This work was supported by the US Department of Energy, Office of Science, Basic Energy Sciences, Chemical Sciences, Geosciences, and Biosciences Division. This research used resources of the Advanced Photon Source, a US Department of Energy (DOE) Office of Science User Facility operated for the DOE Office of Science by Argonne National Laboratory under Contract No. DE-AC02-06CH11357.

References

Bauer, M. (2014). *Phys. Chem. Chem. Phys.* **16**, 13827–13837.
Bergbäck Knudsen, E., Prodi, A., Baltser, J., Thomsen, M., Kjær Willendrup, P., Sanchez del Rio, M., Ferrero, C., Farhi, E., Haldrup, K., Vickery, A., Feidenhans'l, R., Mortensen, K., Meedom Nielsen, M., Friis Poulsen, H., Schmidt, S. & Lefmann, K. (2013). *J. Appl. Cryst.* **46**, 679–696.
Bressler, C., Milne, C., Pham, V.-T., Elnahhas, A., van der Veen, R. M., Gawelda, W., Johnson, S., Beaud, P., Grolimund, D., Kaiser, M., Borca, C. N., Ingold, G., Abela, R. & Chergui, M. (2009). *Science*, **323**, 489–492.
Britz, A., Assefa, T. A., Galler, A., Gawelda, W., Diez, M., Zalden, P., Khakhulin, D., Fernandes, B., Gessler, P., Sotoudi Namin, H., Beckmann, A., Harder, M., Yavaş, H. & Bressler, C. (2016). *J. Synchrotron Rad.* **23**, 1409–1423.
Chen, L., Zhang, X. & Shelby, M. L. (2014). *Chem. Sci.* **5**, 4136–4152.
Chergui, M. & Collet, E. (2017). *Chem. Rev.* **117**, 11025–11065.
Dufresne, E. M., Dunford, R. W., Kanter, E. P., Gao, Y., Moon, S., Walko, D. A. & Zhang, X. (2016). *J. Synchrotron Rad.* **23**, 1082–1086.
Fransson, T., Chatterjee, R., Fuller, F. D., Gul, S., Weninger, C., Sokaras, D., Kroll, T., Alonso-Mori, R., Bergmann, U., Kern, J., Yachandra, V. K. & Yano, J. (2018). *Biochemistry*, **57**, 4629–4637.
Gallo, E. & Glatzel, P. (2014). *Adv. Mater.* **26**, 7730–7746.
Glatzel, P. & Bergmann, U. (2005). *Coord. Chem. Rev.* **249**, 65–95.
Graber, T., Anderson, S., Brewer, H., Chen, Y.-S., Cho, H. S., Dashdorj, N., Henning, R. W., Kosheleva, I., Macha, G., Meron, M., Pahl, R., Ren, Z., Ruan, S., Schotte, F., Šrajer, V., Viccaro, P. J., Westferro, F., Anfinrud, P. & Moffat, K. (2011). *J. Synchrotron Rad.* **18**, 658–670.
Haldrup, K., Vankó, G., Gawelda, W., Galler, A., Doumy, G., March, A. M., Kanter, E. P., Bordage, A., Dohn, A., van Driel, T. B., Kjaer, K. S., Lemke, H. T., Canton, S. E., Uhlig, J., Sundström, V., Young, L., Southworth, S. H., Nielsen, M. M. & Bressler, C. (2012). *J. Phys. Chem. A*, **116**, 9878–9887.
Henke, B., Gullikson, E. & Davis, J. (1993). *At. Data Nucl. Data Tables*, **54**, 181–342.
Ihee, H., Lorenc, M., Kim, T. K., Kong, Q. Y., Cammarata, M., Lee, J. H., Bratos, S. & Wulff, M. (2005). *Science*, **309**, 1223–1227.
Jamula, L. L., Brown, A. M., Guo, D. & McCusker, J. K. (2014). *Inorg. Chem.* **53**, 15–17.
Kastengren, A. (2019). *J. Synchrotron Rad.* **26**, 205–214.
Kern, J., Tran, R., Alonso-Mori, R., Koroidov, S., Echols, N., Hattne, J., Ibrahim, M., Gul, S., Laksmono, H., Sierra, R. G., Gildea, R. J., Han, G., Hellmich, J., Lassalle-Kaiser, B., Chatterjee, R., Brewster, A. S., Stan, C. A., Glöckner, C., Lampe, A., DiFiore, D., Milathianaki, D., Fry, A. R., Seibert, M. M., Koglin, J. E., Gallo, E., Uhlig, J., Sokaras, D., Weng, T.-C., Zwart, P. H., Skinner, D. E., Bogan, M. J., Messerschmidt, M., Glatzel, P., Williams, G. J., Boutet, S., Adams, P. D., Zouni, A., Messinger, J., Sauter, N. K., Bergmann, U., Yano, J. & Yachandra, V. K. (2014). *Nat. Commun.* **5**, 4371.
King, A., Guignot, N., Zerbino, P., Boulard, E., Desjardins, K., Bordessoule, M., Leclerq, N., Le, S., Renaud, G., Cerato, M., Bornert, M., Lenoir, N., Delzon, S., Perrillat, J.-P., Legodec, Y. & Itié, J.-P. (2016). *Rev. Sci. Instrum.* **87**, 093704.
Kraus, P. M., Zürch, M., Cushing, S. K., Neumark, D. M. & Leone, S. R. (2018). *Nat. Rev. Chem.* **2**, 82–94.
Kubin, M., Kern, J., Gul, S., Kroll, T., Chatterjee, R., Löchel, H., Fuller, F. D., Sierra, R. G., Quevedo, W., Weniger, C., Rehanek, J., Firsov, A., Laksmono, H., Weninger, C., Alonso-Mori, R., Nordlund, D. L., Lassalle-Kaiser, B., Glownia, J. M., Krzywinski, J., Moeller, S., Turner, J. J., Minitti, M. P., Dakovski, G. L., Koroidov, S., Kawde, A., Kanady, J. S., Tsui, E. Y., Suseno, S., Han, Z., Hill, E., Taguchi, T., Borovik, A. S., Agapie, T., Messinger, J., Erko, A., Föhlisch, A., Bergmann, U., Mitzner, R., Yachandra, V. K., Yano, J. & Wernet, P. (2017). *Struct. Dyn.* **4**, 054307.
Lancaster, K. M., Roemelt, M., Ettenhuber, P., Hu, Y., Ribbe, M. W., Neese, F., Bergmann, U. & DeBeer, S. (2011). *Science*, **334**, 974–977.
Lee, J. H., Wulff, M., Bratos, S., Petersen, J., Guerin, L., Leicknam, J.-C., Cammarata, M., Kong, Q., Kim, J., Møller, K. B. & Ihee, H. (2013). *J. Am. Chem. Soc.* **135**, 3255–3261.
Lee, N., Petrenko, T., Bergmann, U., Neese, F. & DeBeer, S. (2010). *J. Am. Chem. Soc.* **132**, 9715–9727.

Lengeler, B., Schroer, C. G., Kuhlmann, M., Benner, B., Günzler, T. F., Kurapova, O., Zontone, F., Snigirev, A. & Snigireva, I. (2005). *J. Phys. D Appl. Phys.* **38**, A218–A222.
Lima, F. A., Milne, C. J., Amarasinghe, D. C., Rittmann-Frank, M. H., van der Veen, R. M., Reinhard, M., Pham, V. T., Karlsson, S., Johnson, S. L., Grolimund, D., Borca, C., Huthwelker, T., Janousch, M., van Mourik, F., Abela, R. & Chergui, M. (2011). *Rev. Sci. Instrum.* **82**, 063111.
Madden, H. H. (1981). *J. Vac. Sci. Technol.* **18**, 677–689.
March, A. M., Assefa, T. A., Boemer, C., Bressler, C., Britz, A., Diez, M., Doumy, G., Galler, A., Harder, M., Khakhulin, D., Németh, Z., Pápai, M., Schulz, S., Southworth, S. H., Yavaş, H., Young, L., Gawelda, W. & Vankó, G. (2017). *J. Phys. Chem. C*, **121**, 2620–2626.
March, A. M., Doumy, G., Andersen, A., Al Haddad, A., Kumagai, Y., Tu, M.-F., Bang, J., Bostedt, C., Uhlig, J., Nascimento, D. R., Assefa, T. A., Németh, Z., Vankó, G., Gawelda, W., Govind, N. & Young, L. (2019). *J. Chem. Phys.* Accepted.
March, A. M., Stickrath, A., Doumy, G., Kanter, E. P., Krässig, B., Southworth, S. H., Attenkofer, K., Kurtz, C. A., Chen, L. X. & Young, L. (2011). *Rev. Sci. Instrum.* **82**, 073110.
Martin, T. & Koch, A. (2006). *J. Synchrotron Rad.* **13**, 180–194.
Meents, A., Wiedorn, M. O., Srajer, V., Henning, R., Sarrou, I., Bergtholdt, J., Barthelmess, M., Reinke, P. Y. A., Dierksmeyer, D., Tolstikova, A., Schaible, S., Messerschmidt, M., Ogata, C. M., Kissick, D. J., Taft, M. H., Manstein, D. J., Lieske, J., Oberthuer, D., Fischetti, R. F. & Chapman, H. N. (2017). *Nat. Commun.* **8**, 1281.
Milne, C., Penfold, T. & Chergui, M. (2014). *Coord. Chem. Rev.* **277–278**, 44–68.
Penfold, T. J., Szlachetko, J., Santomauro, F. G., Britz, A., Gawelda, W., Doumy, G., March, A. M., Southworth, S. H., Rittmann, J., Abela, R., Chergui, M. & Milne, C. J. (2018). *Nat. Commun.* **9**, 478.
Pollock, C. J. & DeBeer, S. (2015). *Acc. Chem. Res.* **48**, 2967–2975.
Reininger, R., Liu, Z., Doumy, G. & Young, L. (2015). *J. Synchrotron Rad.* **22**, 930–935.
Ross, M., Andersen, A., Fox, Z. W., Zhang, Y., Hong, K., Lee, J.-H., Cordones, A., March, A. M., Doumy, G., Southworth, S. H., Marcus, M. A., Schoenlein, R. W., Mukamel, S., Govind, N. & Khalil, M. (2018). *J. Phys. Chem. B*, **122**, 5075–5086.
Skuza, J. R., Lukaszew, R. A., Dufresne, E. M., Walko, D. A., Clavero, C., Cebollada, A., Cionca, C. N. & Clarke, R. (2007). *Appl. Phys. Lett.* **90**, 251901.
Smolentsev, G., Soldatov, A. V., Messinger, J., Merz, K., Weyhermüller, T., Bergmann, U., Pushkar, Y., Yano, J., Yachandra, V. K. & Glatzel, P. (2009). *J. Am. Chem. Soc.* **131**, 13161–13167.
Snigirev, A., Kohn, V., Snigireva, I. & Lengeler, B. (1996). *Nature*, **384**, 49–51.
Vankó, G., Bordage, A., Glatzel, P., Gallo, E., Rovezzi, M., Gawelda, W., Galler, A., Bressler, C., Doumy, G., March, A. M., Kanter, E. P., Young, L., Southworth, S. H., Canton, S. E., Uhlig, J., Smolentsev, G., Sundström, V., Haldrup, K., van Driel, T. B., Nielsen, M. M., Kjaer, K. S. & Lemke, H. T. (2013). *J. Electron Spectrosc. Relat. Phenom.* **188**, 166–171.
Vankó, G., Neisius, T., Molnár, G., Renz, F., KÁRPáti, S., Shukla, A. & de Groot, F. M. F. (2006). *J. Phys. Chem. B*, **110**, 11647–11653.
Walko, D. A., Adams, B. W., Doumy, G., Dufresne, E. M., Li, Y., March, A. M., Sandy, A. R., Wang, J., Wen, H. & Zhu, Y. (2016). *AIP Conf. Proc.* **1741**, 030048.
Wullf, M., Plech, A., Eybert, L., Randler, R., Schotte, F. & Anfinrud, P. (2003). *Faraday Discuss.* **122**, 13–26.
Zhang, W., Alonso-Mori, R., Bergmann, U., Bressler, C., Chollet, M., Galler, A., Gawelda, W., Hadt, R. G., Hartsock, R. W., Kroll, T., Kjaer, K. S., Kubiček, K., Lemke, H. T., Liang, H. W., Meyer, D. A., Nielsen, M. M., Purser, C., Robinson, J. S., Solomon, E. I., Sun, Z., Sokaras, D., van Driel, T. B., Vankó, G., Weng, T.-C., Zhu, D. & Gaffney, K. J. (2014). *Nature*, **509**, 345–348.